

Numerical Methods In Cosmological Global Texture Simulations

Julian Borrill

*Blackett Laboratory,
Imperial College of Science and Technology,
Prince Consort Road, London SW7 2BZ, U. K.*

Abstract

Numerical simulations of the evolution of a global topological defect field have two characteristic length scales — one macrophysical, of order the field correlation length, and the other microphysical, of order the field width. The situation currently of most interest to particle cosmologists involves the behaviour of a GUT-scale defect field at the epoch of decoupling, where the ratio of these scales is typically of order 10^{50} . Such a ratio is unrealisable in numerical work, and we consider the approximations which may be employed to deal with this. Focusing on the case of global texture we outline the implementation of the associated algorithms, and in particular note the subtleties involved in handling texture unwinding events. Comparing the results in each approach then establishes that, subject to certain constraints on the minimum grid resolution, the methods described are both robust and consistent with one another.

PACS numbers: 98.80.Cq, 98.70.Vc

1 Introduction

Topological defects as a class of phenomena naturally emerge in the very early universe from the symmetry breaking phase transitions associated with Grand Unifying extensions to the standard $SU(3)_C \otimes SU(2)_L \otimes U(1)_Y$ model of particle physics [1]. A minimal requirement for any theory incorporating such defects is that the energy density in the defect field does not dominate the universe today. In certain cases the defect field is believed to evolve to a scaling regime, wherein its energy density remains a fixed small fraction of the total. Such defects can then be invoked as a possible source of the primordial density perturbations believed to have seeded cosmological structure formation and observed as fluctuations in the cosmic microwave background (CMB) by the COBE satellite [2]. The essential observational constraints on any model of structure formation based on topological defects — most notably invoking either gauged cosmic string [3] or global texture [4] — are therefore of the large scale structure of the local universe essentially as it is now, at a time $t \sim 10^{18}$ s after the big bang, and of the CMB radiation from the epoch of matter/radiation decoupling at $t \sim 10^{13}$ s. By contrast the assumed defect-forming Grand Unified Theory symmetry breaking typically occurs at $t \sim 10^{-35}$ s. Numerical simulations of the evolution and effects of the defect field have therefore come to play an essential role in bridging this gap of some 50 orders of magnitude in time.

A crucial factor determining the type of numerical simulation used is whether the symmetry broken at the phase transition is gauged or global. For a broken gauged symmetry any vacuum field configuration which is not topologically stabilised can simply be trivialised by a suitable gauge transformation, and all that need be considered is the behaviour of the defects themselves which can be treated as discrete objects. For a broken global symmetry however topologically unstable vacuum field configurations are only trivialised by correlation as the field evolves. Since the correlation length of a global defect field is typically taken to be of order the horizon scale its evolution must be followed in detail up to this scale. Cosmological global defect field simulations thus contain two fundamental length scales — one macrophysical, of order the horizon size, and the other microphysical, of order the inverse mass of the field — which we can quantify via their ratio as

$$\mathcal{R} \equiv \frac{L_{macro}}{L_{micro}} \sim \frac{H^{-1}}{M_\phi^{-1}} \quad (1)$$

For a GUT-scale defect at the epoch of decoupling $\mathcal{R} \sim 10^{50}$ and our characteristic length scales again differ by 50 orders of magnitude. Since it is not yet possible to simulate such a range of scales simultaneously we must adopt one of two possible approximation schemes. One approach is to reduce the field's mass scale, and hence increase its width, to a level which is numerically resolvable [5, 6, 7, 8]. Since the field's width characterises the size of the defect core this may be dubbed the expanded core (XCORE) approximation. The alternative is to take the field's mass scale to infinity and hence its width to zero, removing the microphysical scale from the problem [9, 10, 11, 12]. Provided this is done self-consistently the field's equations of motion then reduce to those of the non-linear sigma model (NLSM).

In this paper we consider the implementation of numerical simulations of the evolution of global texture in each of these approaches. In each case the approximated field mass is very different from the physical mass, and it is essential to determine the conditions under

which the resulting simulated evolution still reflects the true behaviour of the field. In the XCORE case some progress has already been made [15] by finding the minimal grid resolution necessary for some of the properties characterising the field’s evolution to asymptote. Here, however, we are able to go further; since the two approaches involve making diametrically opposed approximations consistency between them would be strong evidence that each is close to the true field evolution. Our primary focus therefore is on comparing results from each simulation approach and testing their mutual consistency.

As well as being one of the more promising candidate defect models, global texture also displays some unique features in its evolution. In particular although the texture field is globally topologically trivial, being everywhere on the vacuum manifold with no regions trapped in the false-vacuum phase, it nonetheless admits configurations which are in some sense *locally* topologically non-trivial. In more than two spatial dimensions such configurations are unstable, with their field gradient energy concentrating (by analogy with Derrick’s theorem [13]) until the local energy density is sufficient to pull the field off the manifold and through the false-vacuum, ‘unwinding’ this locally non-trivial topology. Since such unwinding events, where the field leaves the vacuum manifold, are where the different approximation schemes are most likely to diverge, they will provide the most stringent test of consistency.

Having established our notation we commence by detailing the continuum form and discretised implementation of the equations of motion in each approximation scheme. We include in this some discussion of the identification of unwinding events and an analysis of the minimal grid resolution necessary for the approximations to model such events accurately. Working within these constraints we are then able, at least in flat space, to check the simulations against one another. For a number of initial field configurations, both with and without unwinding events, we consider the field’s point-by-point evolution, its gross features, and the CMB anisotropies it generates in each approximation.

2 Notation And Conventions

Except where specified otherwise we consider the evolution of a 4-component real scalar global field Φ in $3 + 1$ dimensional flat space with metric signature $(-, +, +, +)$. This field evolves in a potential of the form

$$V(\Phi) = V_o(|\Phi|^2 - \Phi_o^2)^2 \quad (2)$$

which is defined such that above some critical temperature $\Phi_o^2 < 0$ and the potential has an $O(4)$ symmetry about its minimum at $\Phi = 0$, whilst below it $\Phi_o^2 > 0$ and the symmetry is broken to $O(3)$ about the new minimum which lies somewhere on the entire $S_3 = O(4)/O(3)$ manifold of degenerate vacuum states defined by $|\Phi| = \Phi_o$. This is the simplest symmetry breaking to generate global texture.

In discussing texture configurations it is often useful to parameterise the field at some point in space given by the spherical polar co-ordinates (r, θ, ψ) at some time t as

$$\Phi(r, \theta, \psi, t) = |\Phi|(\cos \mathcal{X}, \sin \mathcal{X} \cos \Theta, \sin \mathcal{X} \sin \Theta \cos \Psi, \sin \mathcal{X} \sin \Theta \sin \Psi) \quad (3)$$

where the group space angles $0 \leq \mathcal{X} < \pi$, $0 \leq \Theta < \pi$ and $0 \leq \Psi < 2\pi$ locate the projection of Φ on the vacuum manifold. In general \mathcal{X} , Θ and Ψ are functions of position and time, although spherically symmetric field configurations can be realised in a particularly simple

way by identifying two of the group space angles with the two physical space angles, $\Theta \equiv \theta$ and $\Psi \equiv \psi$.

For convenience we further normalise the field, $\Phi \rightarrow \Phi/\Phi_0$. All simulations are now performed on lattices with grid spacing δx and using time steps δt and with the speed of light set to $c = 1$ so that grid distances and times are numerically interchangeable. The discretised field is labelled $\Phi_{i,n}$ with i-indices spatial and n-indices temporal.

3 Implementation

3.1 Equations Of Motion

The full texture Lagrangian

$$\mathcal{L} = -\frac{1}{2}\partial^\mu\Phi\partial_\mu\Phi - V_0(|\Phi|^2 - 1)^2 \quad (4)$$

gives the equations of motion of the field as

$$\square\Phi = -\frac{\partial V}{\partial\Phi} \quad (5)$$

In flat space these reduce to

$$\ddot{\Phi} - \nabla^2\Phi = -4V_0(|\Phi|^2 - 1)\Phi \quad (6)$$

Using a standard staggered leapfrog method [14] these can be discretised to second order to yield

$$\begin{aligned} \dot{\Phi}_{i,n+1/2} &= \dot{\Phi}_{i,n-1/2} + \left(\nabla^2\Phi_{i,n} - 4V_0(\Phi_{i,n}^2 - 1)\Phi_{i,n}\right)\delta t \\ \Phi_{i,n+1} &= \Phi_{i,n} + \dot{\Phi}_{i,n+1/2}\delta t \end{aligned} \quad (7)$$

These are the equations used in the XCORE approximation.

Alternatively, imposing the NLSM approximation and restricting the field to remain on the vacuum manifold at all times, the constrained Lagrangian can be written

$$\mathcal{L} = -\frac{1}{2}\partial^\mu\Phi\partial_\mu\Phi - \frac{\sigma}{2}(|\Phi|^2 - 1) \quad (8)$$

where σ is a Lagrange multiplier. The equations of motion now become

$$\square\Phi = \sigma\Phi \quad (9)$$

giving

$$\sigma = (\square\Phi) \cdot \Phi \quad (10)$$

Using the constraint to solve this equation for σ the flat space equations become

$$\ddot{\Phi} - \nabla^2\Phi = -(\dot{\Phi}^2 - \nabla\Phi^2)\Phi \quad (11)$$

Again discretising to second order these give

$$\Phi_{i,n+1} = 2\Phi_{i,n} - \Phi_{i,n-1} + \nabla^2\Phi_{i,n}\delta t^2 - (\dot{\Phi}_{i,n}^2 - \nabla\Phi_{i,n}^2)\delta t^2\Phi_{i,n} \quad (12)$$

Following Pen et al [10] this can be cast in the form

$$\Phi_{i,n+1} = \lambda\Phi_{i,n} + \delta\Phi_{i,n} \quad (13)$$

where

$$\begin{aligned} \delta\Phi_{i,n} &= \Phi_{i,n} - \Phi_{i,n-1} + \nabla^2\Phi_{i,n}\delta t^2 \\ \lambda &= 1 - (\dot{\Phi}_{i,n}^2 - \nabla\Phi_{i,n}^2)\delta t^2 \end{aligned} \quad (14)$$

Using the constraint $|\Phi_{i,n+1}| = 1$ to solve for λ now gives

$$\lambda = -\delta\Phi_{i,n}\cdot\Phi_{i,n} \pm \sqrt{1 - \delta\Phi_{i,n}^2 + (\Phi_{i,n}\cdot\delta\Phi_{i,n})^2} \quad (15)$$

and we are able to circumvent the numerically troublesome squared derivative terms. Note that to first order in δt equation (13) is

$$\Phi_{i,n+1} = \pm\Phi_{i,n} + O(\delta t) \quad (16)$$

with the choice of sign coming from the choice of root in equation (15); taking the negative root, so that $\Phi_{i,n+1} \sim -\Phi_{i,n}$, therefore explicitly introduces an unwinding event at the given gridpoint.

3.2 Unwinding Events

Evolving the texture field on a discrete lattice there are two types of unwinding event. If the initial field conditions are sufficiently symmetric about some gridpoint that the group space angles there are time-independent then an unwinding can occur at that gridpoint. However for more random initial field conditions the unwinding site will not lie exactly at a gridpoint. To investigate the properties of individual texture unwindings, as well as to test the accuracy of our simulations generally, we would like to be able to identify both types of event unambiguously.

The full texture field equations of motion include unwinding events dynamically. Reducing the mass scale of the field allows it to be pulled off the vacuum manifold more easily, so that making the XCORE approximation increases the volume of space leaving the vacuum and forming the defect core. The constraint on the field mass is then that it should be sufficiently small that any unwinding event will pull the field below some threshold value — typically taken as $|\Phi_{i,n}| < 0.5$ — throughout a volume containing at least one gridpoint. Conversely the mass must also be large enough that the field is only pulled below this threshold at unwinding events. However, since we are trying to maximise the range of length scales, and hence require as large a mass as possible, only the upper limit serves as a serious restriction. A further constraint on the field's mass comes from the upper limit on field gradients imposed by the finite grid spacing; if the width is too small then even unwindings occurring at gridpoints can be inhibited by the resulting upper limit on the field's gradient energy density. A detailed investigation of these constraints [15] leads to a practical lower limit on the field width

$$W \geq 0.25 \delta x \quad (17)$$

Subject to this, and the grid resolution conditions discussed below, the threshold prescription serves to identify unwindings in the XCORE approximation.

Since the NLSM approximation constrains the field to remain on the vacuum manifold at all times it is unable to admit unwinding events in the continuum. However, as demonstrated above, the discretised equations of motion include a means by which an unwinding can be explicitly re-introduced at a given gridpoint. All that remains is to determine the appropriate criteria under which such an unwinding should be incorporated in the field's evolution. For diagrammatic simplicity in the remainder of this section we consider the case of a 3-component NLSM texture field in $2 + 1$ dimensions where the vacuum manifold is S_2 .

The most obvious approach is to introduce an unwinding at any gridpoint in the immediate vicinity of which the field covers more than half of the vacuum manifold — ie. if we consider the bisection of the manifold by the closed boundary on it given by joining the nearest neighbours to any gridpoint along geodesics then we introduce an unwinding whenever the field at the gridpoint lies in the larger of the two sub-sections. To date the only attempt to implement this criterion [10, 11] involves calculating the mean value of the (here 4) nearest neighbours to a gridpoint, $\bar{\Phi}_{i,n}$, and introducing an unwinding if and only if $\Phi_{i,n} \cdot \bar{\Phi}_{i,n} < 0$. This is equivalent to replacing the actual boundary on the manifold with an ‘averaged’ one defined by the intersection of the manifold with the plane perpendicular to $\bar{\Phi}_{i,n}$ (figure 1). Note that without loss of generality we can always take $\bar{\Phi}_{i,n}$ to point ‘south’, whereupon $\Phi_{i,n} \cdot \bar{\Phi}_{i,n} < 0$ if and only if $\Phi_{i,n}$ and $\bar{\Phi}_{i,n}$ lie in opposite hemispheres.

In the symmetric case it is straightforward to show that

$$\bar{\Phi}_{i,n} \propto \Phi_{i,n} \quad (18)$$

and hence that $\Phi_{i,n}$ and $\bar{\Phi}_{i,n}$ lie in opposite hemispheres if and only if more than half of the vacuum manifold is covered locally (figure 2).

For non-symmetric configurations this approach breaks down in a number of ways:

- since in general $\bar{\Phi}_{i,n} \not\propto \Phi_{i,n}$ it is simple to construct configurations where $\Phi_{i,n}$ and $\bar{\Phi}_{i,n}$ lie in the same hemisphere but which should nonetheless be unwound (figure 3). As is clear from this example the correct condition for identifying an unwinding is instead $(\Phi_{i,n} - \bar{\Phi}_{i,n}) \cdot \bar{\Phi}_{i,n} < 0$.
- if the field at the gridpoint in question lies between the true boundary and the ‘average’ boundary then even the correct condition either mistakenly identifies or fails to identify an unwinding configuration (figure 4).
- since in general the unwinding site is not at a gridpoint even if the algorithm correctly identifies a configuration that should unwind what we are doing in effect is unwinding the gridpoint closest to the actual unwinding site. However in the NLSM approximation *only* at the unwinding site itself should the field ever leave the vacuum manifold. Moreover, even if the NLSM condition is relaxed and a small region of space close to the unwinding site (and including the gridpoint) is allowed to leave the manifold it is only at the unwinding site itself that the field is approximately inverted, $\Phi_{i,n+1} \sim -\Phi_{i,n}$. This approach therefore incorrectly evolves the field at the gridpoint, and can thereby generate a repeated unwinding (figure 5).

In practice unless the unwinding site is fixed at a gridpoint (when the required symmetry avoids the above difficulties) it is unnecessary to explicitly unwind the field at all, since the geodesic assumption (that between neighbouring points the field follows a geodesic on the manifold) implicitly unwinds any configuration locally covering more than half the manifold anyway. However the problem of unambiguously identifying unwindings in the NLSM approximation in order to study their properties remains unsolved.

3.3 Grid Resolution

Given the above microphysical length scales, the resolution afforded by a particular simulation lattice can be quantified by the number of gridpoints N_l corresponding to the initial macrophysical length scale. For comparison between different approaches we need a length scale which is well-defined and which can be meaningfully implemented in all simulations — for example in flat space the horizon is not well-defined, whilst symmetric initial field configurations have an infinite correlation length.

A necessary condition for any field configuration to unwind that to do so must reduce the gradient energy in the configuration, and hence that it should cover more than half of the vacuum manifold before unwinding, and by corollary less than half afterwards. Therefore, as in previous work [7, 8], we adopt as our macrophysical length scale the radius of a sphere within which no more than half of the manifold can possibly be covered initially. For singly-wound spherically symmetric configurations [7] the manifold covering about the origin is given (in the ansatz of equation (3)) by

$$Q(r) = \frac{1}{\pi} \left(\mathcal{X}(r) - \frac{1}{2} \sin 2\mathcal{X}(r) \right) \quad (19)$$

and our length scale is the radius at which $Q = 0.5$ initially. For interpolated random configurations [8] it is half the distance between gridpoints at which the initial field values are randomly assigned.

Figure 6 illustrates the variation in the topological charge causally associated with the unwinding of a spherically symmetric configuration in flat space $Q(t_{uw} - t_o)$ (where t_{uw} and t_o are the unwinding and initial times respectively), with the grid resolution N_l in each approximation. To get within 10% of the asymptotic result in both simulations simultaneously a lower limit on the number of gridpoints per half-manifold radius in flat space is $N_l \geq 5$, and to within 5%, $N_l \geq 10$. However it should be stressed that these results *only* apply to spherically symmetric configurations in flat space. Experiments using the XCORE approximation in expanding backgrounds and with random configurations demonstrate that in such circumstances the minimum resolution is increased [15], and wherever possible the simulations presented here satisfy the tighter constraint from that work, $N_l \geq 16$.

4 Comparison

The evolution of an initial field configuration under each of the approximations can be compared in a number of ways; here we consider three levels of consistency. Firstly we can calculate point by point statistics measuring the correlation of the field over the lattice at every time step. Alternatively we can consider the consistency of any gross features of the

simulations, such as the times and locations of any identifiable unwinding events. Finally we can compare observable consequences of the field evolutions, such as their induced CMB anisotropies. Clearly these levels of consistency are hierarchical; if the simulations are consistent point by point then their gross features and physical consequences will be identical. Similarly even if their point by point evolution varies, provided the gross features are the same then we might expect the induced CMB anisotropies to be so too.

4.1 Pointwise Statistics

Given that the vacuum manifold is the 3-sphere $|\Phi| = 1$ a simple measure of the correlation of the field at any point and time is given (in an obvious notation) by

$$\xi_{i,n} = \Phi_{i,n}^X \cdot \Phi_{i,n}^N \quad (20)$$

However we know at the outset that differences will emerge as the simulations progress simply because the field is able to leave the vacuum manifold in the XCORE but not in the NLSM approximation. As a further comparison therefore we can factor out this effect by comparing the normalised fields, projecting the XCORE field back onto the vacuum manifold everywhere

$$\hat{\xi}_{i,n} = \frac{\Phi_{i,n}^X}{|\Phi_{i,n}^X|} \cdot \Phi_{i,n}^N \quad (21)$$

In this way we can determine the relative importance in any absence of correlation of differences in the field positions' magnitudes and of differences in their orientations.

Symmetric configurations are artificially self-correlated on all scales at all times, possibly enhancing their cross-correlation too, so we focus on the evolution of random configurations alone. Using a catalogue of random initial configurations admitting unwinding events [8] we take a sample of 22 configurations, equally divided between ones with and ones without an unwinding. These are then simultaneously evolved on a pair of 48^3 lattices for 24 grid time units. Running the simulations simultaneously restricts us to half the usual grid size (and hence resolution) here, so the results should be taken as upper limits which would be reduced were it possible to work at full resolution. We calculate as our correlation statistic the mean values of each measure over the simulation lattice at each timestep

$$\xi_n = \frac{1}{N} \sum_{i=1}^N \xi_{i,n} \quad \hat{\xi}_n = \frac{1}{N} \sum_{i=1}^N \hat{\xi}_{i,n} \quad (22)$$

Exact correlation gives a statistic of 1, anti-correlation -1, and no correlation 0. In all simulations and at every timestep we find $\xi_n = \hat{\xi}_n = 1.0$.

To test of the degree of this consistency we also note the number and distribution of gridpoints at which either of the correlation measures falls below 0.9. In simulations of both unwinding and non-unwinding configurations gridpoints whose fields are less than 90% correlated are found localised in time and space about events during which the field is pulled significantly off the manifold in the XCORE simulations. This is true both for the known unwinding events, and for the non-unwinding events (at which insufficient gradient energy collapses to unwind the field) which may be identified *post hoc* by the characteristic CMB anisotropy pattern they induce [16]. However, these imperfectly correlated regions are very

small; even the largest region involves less than 0.1%, and a typical region less than 0.01%, of the simulation gridpoints.

Figure 7 shows the variation in the number of gridpoints whose fields are less than 90% correlated under each measure as the simulation progresses for a typical configuration, in this case including an unwinding at grid time 13.9. We see that for the full field the number of imperfectly correlated points peaks just before and after the unwinding event, but that only a small fraction of this discrepancy is due to differences in orientation, and that these differences peak at the unwinding itself. The sequence of post-unwinding peaks in the full field correlation measure is to be expected given the suppression of the damping of radial oscillations by the reduction in the field’s mass in the XCORE approximation. Note that, except for the first, these peaks involve a single point; explicit examination of the simulation confirms that this is indeed the site of the unwinding event.

4.2 Gross Field Features

As shown above the only even marginally uncorrelated sections of the simulations are associated with unwinding or non-unwinding events. We now consider the extent to which the gross features of these events, such as their time and place, reflect this and differ between the simulations. The cross-correlation results already limit the possible differences; in each case the event must occur within the imperfectly correlated region of simulation spacetime, so their locations cannot differ by more than the size of this region.

As a more precise test we can attempt to identify and thereby locate each simulations’ unwinding and non-unwinding events explicitly. The unwinding events are identified in the XCORE simulation as occurring at the gridpoint at which the magnitude of the field falls below some threshold, $|\Phi| < 0.5$, and at the time half way between its first falling below the threshold and subsequently exceeding it again. In the NLSM simulations we use the criterion discussed above, $(\Phi_{i,n} - \bar{\Phi}_{i,n}) \cdot \bar{\Phi}_{i,n} < 0$, whilst acknowledging its weaknesses. Note that the criterion is used simply to identify candidate unwinding events, and the equations of motion are unchanged, with the positive root being taken in equation (15). Where unwindings are successfully identified (in all but one case) they are found to occur at the same gridpoint and within 0.5 grid time units of their XCORE counterparts.

Identification of non-unwinding events is less precise; in both XCORE and NLSM simulations we look for the characteristic CMB signature — a sharply peaked cold spot followed by a similar hot spot [16]. By analogy with unwindings, the non-unwinding event is then taken to occur at the gridpoint around which the peaks are centred and at the time at which the cold to hot spot transition occurs. In every case the event occurs at the same gridpoint and on the same photon sheet. Since the sheets are separated by 1 grid spacing this specifies the event’s time again to within 0.5 grid time units.

4.3 CMB Anisotropies

Finally we compare the CMB anisotropies induced by the texture field’s evolution in each simulation. The details of the method are described elsewhere [16]; in essence we send a sheet of photons across a lattice over which the texture field is evolving and calculate the ‘kick’ given to each photon at each time step in the stiff source, small angle approximation [17]. The variation in the CMB temperature across the sheet is then recovered by Fourier analysis.

Here we are interested in the difference in the temperature anisotropies induced by a given initial field configuration evolved in each approach; we calculate

$$\delta T = \frac{1}{N} \sum_{i=1}^N ((\Delta T/T)_i^X - (\Delta T/T)_i^N) \quad (23)$$

where the sum is over a given sheet of photons. For all configurations and for every sheet $\delta T = 0$. However the standard deviation of the temperature difference across the sheets clearly differs between the unwinding and non-unwinding configurations. Taking $\epsilon = 8\pi^2 G\Phi_0^2$, the magnitude of the anisotropy generated by the one known analytic solution to the flat space NLSM equations [18], we find

$$\sigma \leq \begin{cases} 0.05 \epsilon & \text{unwinding} \\ 0.01 \epsilon & \text{non-unwinding} \end{cases} \quad (24)$$

Since the characteristic CMB anisotropy generated by an unwinding or non-unwinding event involves a sharply peaked cold spot being succeeded by a similar hot spot we can also consider differences in the maximum and minimum anisotropies between simulation pairs. We calculate

$$\delta T_{\max} = \frac{1}{N} \sum_{i=1}^N ((\Delta T/T)_{\max}^X - (\Delta T/T)_{\max}^N) \quad (25)$$

and

$$\delta T_{\min} = -\frac{1}{N} \sum_{i=1}^N ((\Delta T/T)_{\min}^X - (\Delta T/T)_{\min}^N) \quad (26)$$

where the sum is now taken over the set of all unwinding or all non-unwinding simulations, and now find

$$\begin{aligned} \delta T_{\max} &= \begin{cases} (-0.02 \pm 0.04) \epsilon & \text{unwinding} \\ (-0.03 \pm 0.03) \epsilon & \text{non-unwinding} \end{cases} \\ \delta T_{\min} &= \begin{cases} (-0.04 \pm 0.04) \epsilon & \text{unwinding} \\ (-0.02 \pm 0.02) \epsilon & \text{non-unwinding} \end{cases} \end{aligned} \quad (27)$$

where the error bars are 1σ . Thus it appears that on average the NLSM gives marginally stronger peaks than the XCORE simulations, although in all cases the difference is within 1σ . Indeed the only consistent discriminant between the anisotropies generated in each simulation is that the difference in individual peak heights $(\Delta T/T)_{\max} - (\Delta T/T)_{\min}$ is in every case slightly greater in the NLSM simulation than its XCORE counterpart, although never by more than 0.1ϵ .

5 Conclusions

We have detailed the implementation of two approaches to circumventing the problem of the range of scales inherent in numerical simulations of global defect fields. It is to be expected that each approach will be constrained by a minimum lattice resolution, and that

such constraints will be strongest whenever significant events occur on microphysical length scales. In the case of global texture such events are the unwindings and non-unwindings associated with the local concentration of field gradient energy. We find that there is indeed a minimum resolution — of the order of 5 grid spacings per initial half-manifold radius — for such events to be modelled accurately for spherically symmetric simulations in flat space.

For non-symmetric field configurations we have been unable to improve on the previously established resolution limits [15] because of the difficulty of unambiguously identifying unwinding events in NLSM simulations of non-symmetric field configurations. The naive approach to this problem is shown to be flawed in several ways, although the consequences for work in which it is used [10, 11] are unclear. It would certainly be possible to examine the effect of adopting inappropriate unwinding criteria on our single-texture simulations. However because of the fundamental differences — particularly in the grid resolution — between these and the many-texture simulations in which such unwinding criteria are used it would be difficult to meaningfully extrapolate any effect from one to the other.

Working subject to these constraints we have been able directly to compare the evolution of a set of initial field configurations in each approach. In every case the fields are very strongly correlated, with what little discrepancy there is being almost entirely radial and simply reflecting the ability of the XCORE field to leave the vacuum manifold. Moreover, even where such discrepancies occur the subsequent return to near-perfect correlation indicates that the simulations are stable to them. Given this consistency it is not surprising that, insofar as we are able to identify them and to the accuracy of the identification schemes, all the unwinding and non-unwinding events occur at the same grid places and times in each approach. The fact that the fields remain so well correlated throughout the simulations also implies that the temporal derivatives of the field are equally consistent. Since the evolution of the velocity field that generates the CMB anisotropies their consistency — both absolutely, over individual simulations, and even more so statistically, over sets of simulations — is likewise a reflection of the correlation of the velocity fields.

In conclusion we find that, subject to using a sufficiently fine lattice and a careful handling of the discontinuity inherent in the NLSM approach at unwinding, the XCORE and NLSM approaches to the simulation of the evolution of global texture are entirely consistent with one another, and hence may both be taken to give good representations of the true field evolution.

Acknowledgements

The author acknowledges the support of the SERC, and wishes to thank Ed Copeland, Andrew Liddle, Albert Stebbins and Shoba Veeraraghavan for helpful discussions.

References

- [1] T.W.B. Kibble, *J. Phys.* **A9**, 1387 (1976).
- [2] G. F. Smoot *et al*, *Astrophys. J. Lett.* **396**, L1 (1992).

- [3] G. Gibbons, S. Hawking and T. Vachaspati (eds) *The Formation And Evolution Of Cosmic Strings* (Cambridge, 1990).
A. Albrecht and A. Stebbins, Phys. Rev. Lett. **68**, 2121 (1992).
- [4] R. Davis, Phys. Rev. D**35** 3705 (1987); **36** 997 (1987).
N. Turok, Phys. Rev. Lett. **63**, 2625 (1989).
- [5] W. H. Press, B. S. Ryden and D. N. Spergel, Astrophys. J. **347**, 590 (1989).
- [6] D. N. Spergel, N. Turok, W. H. Press and B. S. Ryden, Phys. Rev. D**43**, 1038 (1991).
- [7] J. Borrill, E. J. Copeland and A. R. Liddle, Phys. Rev. D**46**, 524 (1992).
- [8] J. Borrill, E. J. Copeland and A. R. Liddle, Phys. Rev. D**47**, 4292 (1993).
- [9] D. P. Bennett and S. H. Rhie, Astrophys. J. Lett. **406**, L7 (1993).
- [10] U.-L. Pen, D. N. Spergel and N. Turok, Phys. Rev. D**49**, 692 (1994).
- [11] D. Coulson, U.-L. Pen and N. Turok, ‘Degree Scale Microwave Anisotropies in Non-Gaussian theories of Cosmic Structure Formation’, Princeton preprint PUP-TH-93/1393 (1993).
D. Coulson, P. Ferreira, P. Graham and N. Turok, “Microwave Anisotropies from Cosmic Defects”, Nature, in press (1994).
- [12] R. Durrer and D. N. Spergel, in “Trends in Astroparticle Physics” ed. D Cline & R. Peccei, World Scientific (Singapore) (1992).
R. Durrer, A. Howard and Z-H Zhou, Phys. Rev. D**49** 681 (1994).
- [13] G. H. Derrick, J. Math. Phys. **5** 1252 (1964).
- [14] W. H. Press, B. P. Flannery, S. A. Teukolsky and W. T. Vetterling, *Numerical Recipes* (Cambridge University Press, 1986)
- [15] J. Borrill, Phys. Rev. D**47**, 4298 (1993).
- [16] J. Borrill, E. J. Copeland, A. R. Liddle, A. Stebbins and S. Veeraraghavan, “Texture-Induced Microwave Background Anisotropies”, Imperial College preprint IMPERIAL/TP/93-94/21 (1994).
- [17] A. Stebbins, Astrophys. J., **327**, 584 (1988).
- [18] N. Turok and D. N. Spergel, Phys. Rev. Lett. **64**, 2736 (1990).

Figure Captions

Figure 1

a) Working on a 2-dimensional lattice consider each gridpoint i (empty dot) and its 4 nearest neighbours (filled dots) at time step n .
b) Mapping the gridpoint and its neighbours onto the manifold the bisecting boundary is constructed by connecting the neighbours along geodesics (dotted line). An unwinding should now be re-introduced whenever the field at the given gridpoint $\Phi_{i,n}$ lies in the larger sub-section of the thus bisected manifold. The approximation considered here is now to replace the actual boundary with the ‘average’ boundary given by the intersection of the manifold with the plane perpendicular to the mean value of the neighbours $\bar{\Phi}_{i,n}$ (heavy line). Each boundary bisects the manifold into two distinct sub-sections.

Figure 2

For sufficiently (for example spherically) symmetric configurations $\bar{\Phi}_{i,n}$ is always parallel to $\Phi_{i,n}$, so $\Phi_{i,n} \cdot \bar{\Phi}_{i,n} < 0$ if and only if $\Phi_{i,n}$ lies in the larger manifold sub-section — a) no unwinding, b) unwinding. In this case $\Phi_{i,n}$ and $\bar{\Phi}_{i,n}$ being in different hemispheres is exactly equivalent to $\Phi_{i,n}$ lying in the larger sub-section.

Figure 3

In general $\bar{\Phi}_{i,n}$ is not parallel to $\Phi_{i,n}$, and the equivalence noted in the symmetric case breaks down. Now $\Phi_{i,n}$ can be in the same hemisphere as $\bar{\Phi}_{i,n}$ whilst remaining in the larger manifold sub-section. However replacing $\Phi_{i,n}$ with $\Phi_{i,n} - \bar{\Phi}_{i,n}$ restores the equivalence, so the corrected unwinding criterion becomes $(\Phi_{i,n} - \bar{\Phi}_{i,n}) \cdot \bar{\Phi}_{i,n} < 0$.

Figure 4

The approximation of replacing the true boundary with the ‘average’ boundary breaks down whenever $\Phi_{i,n}$ lies between the two.

- (a) if $\Phi_{i,n}$ is in the smaller true sub-section but the larger ‘average’ sub-section then an unwinding will be mistakenly included.
- (b) if $\Phi_{i,n}$ is in the larger true sub-section but the smaller ‘average’ sub-section then an unwinding will be missed.

Figure 5

The unwinding of a point other than the exact unwinding site in this prescription, where the field is unwound by (to first order) being inverted, $\Phi_{i,n+1} \sim -\Phi_{i,n}$, is clearly incorrect. For example there are configurations in which, if the neighbouring points do not evolve significantly, the unwound field remains in the larger manifold sub-section, and so re-unwinds.

Figure 6

The variation in the topological charge Q causally associated with the unwinding of a spherically symmetric texture field configuration with the grid resolution parameter N_l in both the XCORE (solid line) and NLSM (solid line) approximations.

Figure 7

The variation in the number of gridpoints less than 90% correlated between the XCORE and NLSM simulations of a typical random field configuration with run time. Both the full fields (solid line) and the normalised fields (dashed line) are compared. An unwinding event occurs in at grid time 13.9.

This figure "fig1-1.png" is available in "png" format from:

<http://arxiv.org/ps/astro-ph/9403006v1>

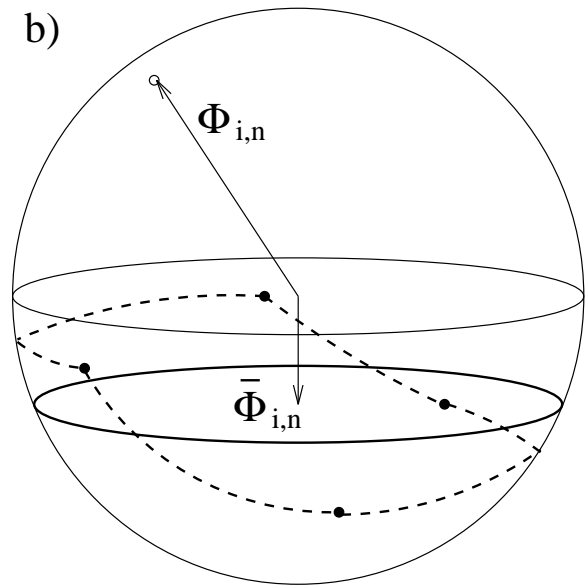
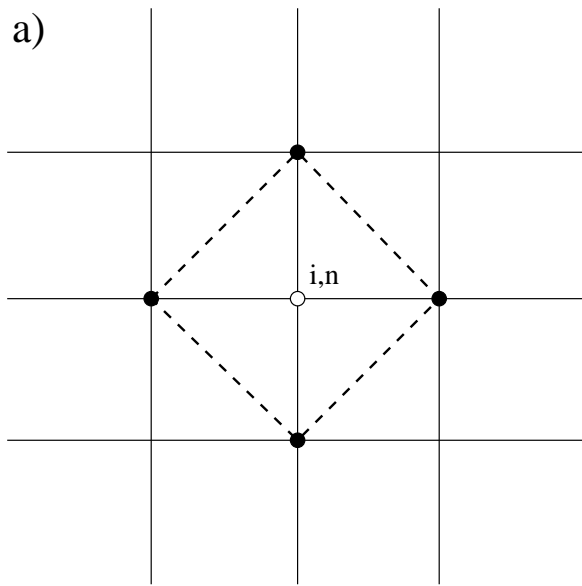


FIGURE 1

This figure "fig1-2.png" is available in "png" format from:

<http://arxiv.org/ps/astro-ph/9403006v1>

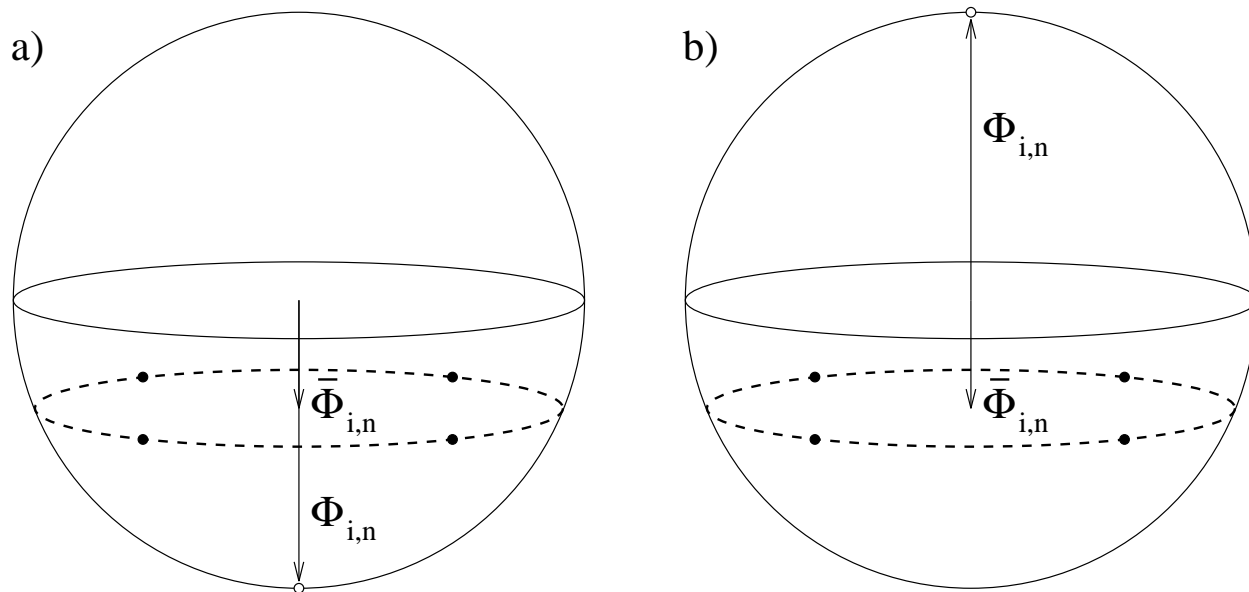


FIGURE 2

This figure "fig1-3.png" is available in "png" format from:

<http://arxiv.org/ps/astro-ph/9403006v1>

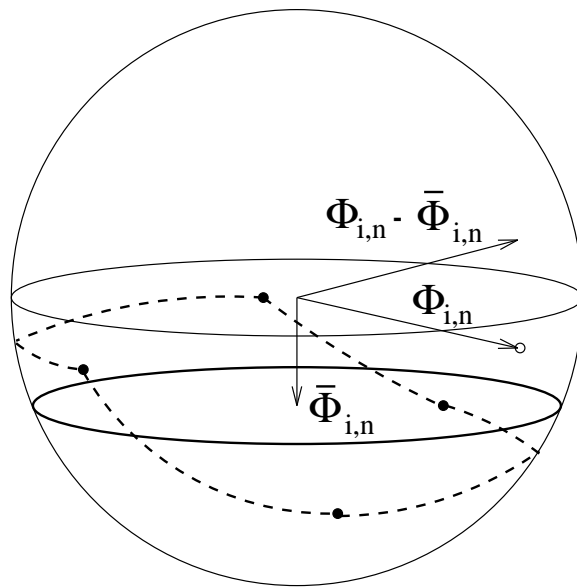


FIGURE 3

This figure "fig1-4.png" is available in "png" format from:

<http://arxiv.org/ps/astro-ph/9403006v1>

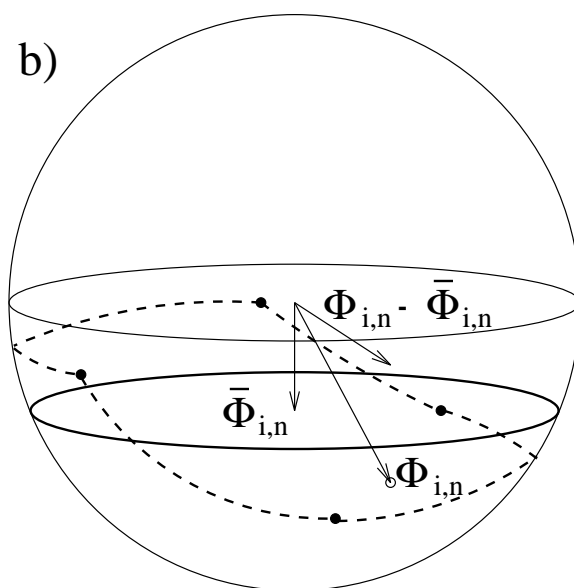
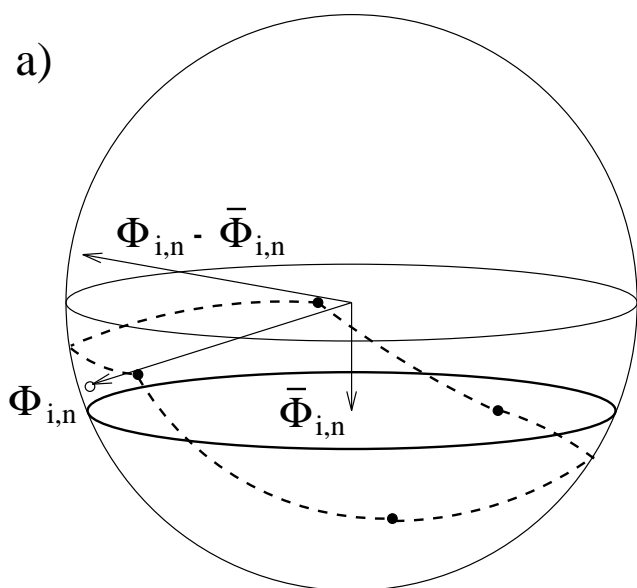


FIGURE 4

This figure "fig1-5.png" is available in "png" format from:

<http://arxiv.org/ps/astro-ph/9403006v1>

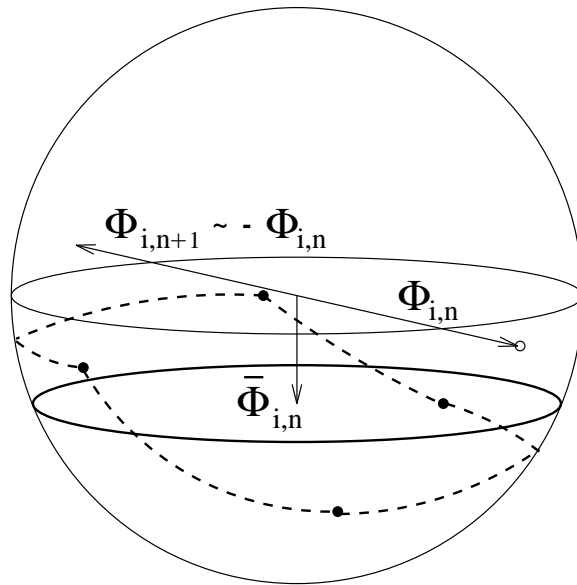
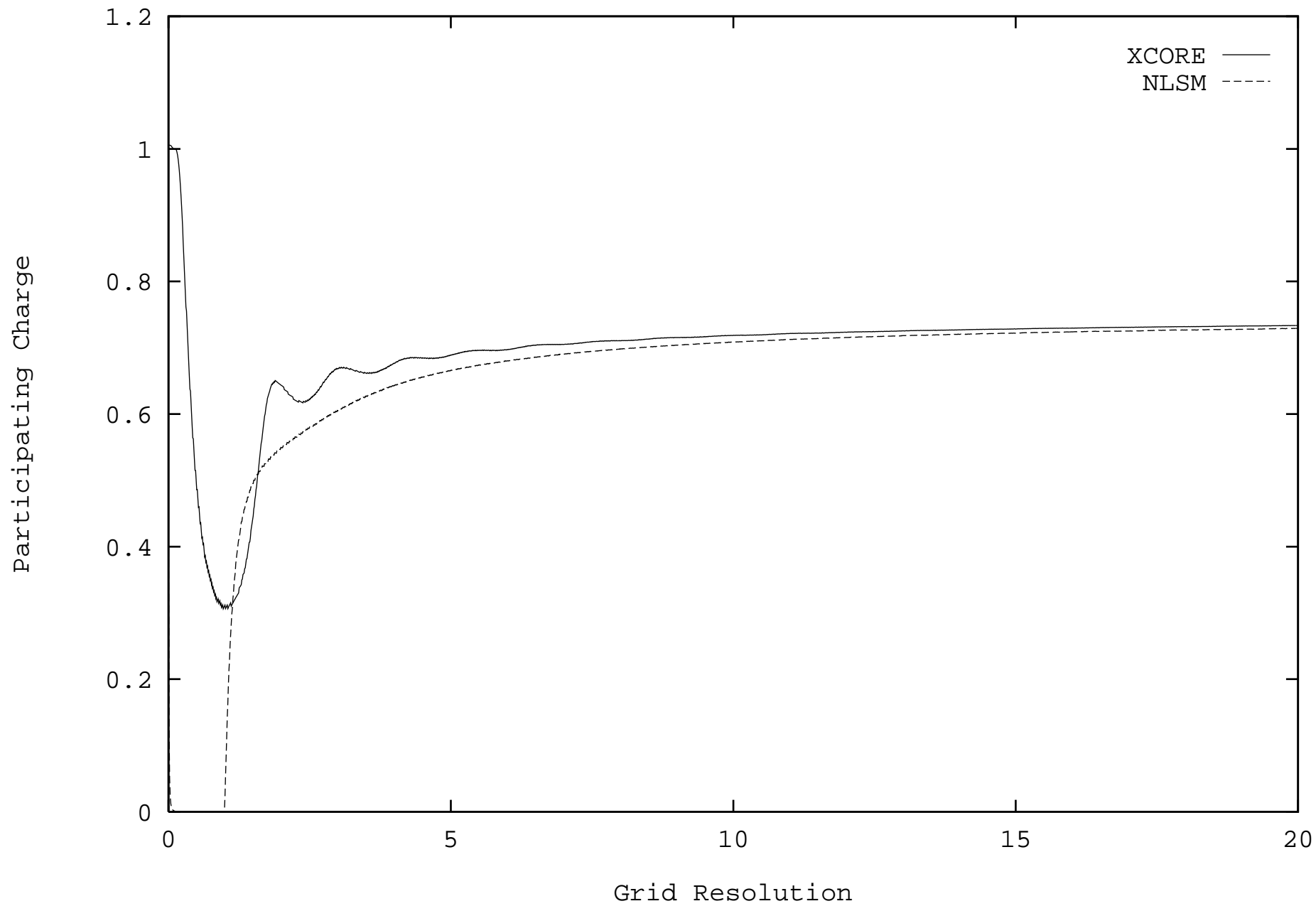


FIGURE 5

This figure "fig1-6.png" is available in "png" format from:

<http://arxiv.org/ps/astro-ph/9403006v1>

FIGURE 6



This figure "fig1-7.png" is available in "png" format from:

<http://arxiv.org/ps/astro-ph/9403006v1>

FIGURE 7

